
Joint Denoising of Cryo-EM Projection Images using Polar Transformers

Joakim Andén

KTH Royal Institute of Technology
Flatiron Institute, Simons Foundation
janden@kth.se

Justus Sagemüller

KTH Royal Institute of Technology
justussa@kth.se

Abstract

Deep neural networks (DNNs) have proven powerful for denoising, but they are ultimately of limited use in high-noise settings, such as for cryogenic electron microscopy (cryo-EM) projection images. In this setting, however, datasets contain a large number of projections of the same molecule, each taken from a different viewing direction. This redundancy of information is useful in traditional denoising techniques known as class averaging methods, where images are clustered, aligned, and then averaged to reduce the noise level. We present a neural network architecture based on transformers that extends these class averaging methods by simultaneously clustering, aligning, and denoising cryo-EM images. Results on synthetic data show accurate denoising performance using this architecture, reducing the relative mean squared error (MSE) single-image DNNs by 45% at a signal-to-noise (SNR) of 0.03.

1 Introduction

Many imaging problems amount to reconstructing some unknown quantity (often two-dimensional images or three-dimensional density maps) from several measurements obtained through a lossy, noisy forward process. One such problem is single-particle cryogenic electron microscopy (cryo-EM) (Dubochet et al., 1982), a molecular imaging technique that uses transmission electron microscopes to analyze the structure of molecules, typically proteins of interest for biological or medical research. This involves freezing a sample containing millions of copies of a single molecule in a thin layer of vitreous ice, imaging the frozen sample in an electron microscope, and then reconstructing the 3D structure of the molecule from the resulting 2D projection images, known as *micrographs*. The reconstruction process involves several steps, such as first extracting images of individual particles from the micrographs, denoising these images, constructing a low-resolution initial reference map, and then refining this into the final 3D density map (Frank, 1996).

An important challenge of cryo-EM imaging is the high noise level. Indeed, since the electron dose is kept low to avoid radiation damage, each projection contains only a weak signal and a large amount of shot noise (Bendory et al., 2020). Denoising is therefore a central task in any cryo-EM pipeline. For example, it is needed for visual inspection (Singer & Sigworth, 2020), detecting contamination (outliers) (Bhamre et al., 2016), generating templates for particle picking (Singer & Sigworth, 2020), identifying high-quality projection images (Scheres, 2015), and as preprocessing for certain ab-initio reconstruction methods (Singer & Shkolnisky, 2011).

Traditional denoising methods can be divided into two categories. The first is based on applying a Wiener filter to the images (Frank et al., 1996; Tang et al., 2007; Sindelar & Grigorieff, 2011; Bhamre et al., 2016). While this approach exploits prior information on the content of the images and is optimal in the class of linear estimators, it often results in a high level of blurring for the

relevant noise levels. The second group of conventional denoising methods is known collectively as *class averaging* methods. These rely on the geometry of the problem described above – given the large number of images, they can be divided into clusters having approximately the same viewing direction up to in-plane rotation. Class averaging methods therefore first classify the images, where each cluster consists of images that are similar up to some in-plane rotation, then align those images rotationally and average them (van Heel, 1984; Park & Chirikjian, 2014; Zhao & Singer, 2014a; Scheres, 2015). This average has less noise, no bias introduced by a filter, and can then be used for subsequent reconstruction tasks. However, the high noise level makes both classification and alignment very challenging (Jensen, 2001).

Like many other disciplines, cryo-EM processing has been improved in several ways by the introduction of methods from deep learning. This ranges from particle picking (Wang et al., 2016; Wagner et al., 2019) and postprocessing of 3D densities (Sanchez-Garcia et al., 2021) to implicit neural representations for 2D images (Bibas et al., 2021; Nasiri & Bepler, 2022; Kwon et al., 2023) and 3D structures (Zhong et al., 2021; Nashed et al., 2021; Levy et al., 2022; Schwab et al., 2024). DNNs have also been used for denoising, but in the setting of entire micrographs (Bepler et al., 2020; Buchholz et al., 2019; Palovcak et al., 2020). This problem is different from the denoising of projection images in several respects, such only being able to leverage information within a single micrograph. These methods also do not explicitly incorporate rotational symmetries of the data distribution, limiting their performance.

This work proposes to solve the denoising problem by simultaneously denoising multiple images in a manner that extends traditional class averaging by leveraging prior information on the content of the projection images. The novel architecture rotationally aligns and integrates information from multiple cryo-EM projection images using a new convolutional attention mechanism that also guarantees the overall rotational equivariance of the system. This network, known as *polar transformer*, is shown to successfully cluster, align, and denoise sets of cryo-EM images on simulated datasets, yielding a reduction of 45% in relative mean squared error (MSE) compared to deep neural networks operating on single projections of signal-to-noise ratio (SNR) as low as 0.03.

The rest of this paper is structured as follows. Section 2 describes the three main denoising tasks: single-image denoising, directional set denoising, and general set denoising. Then Section 3 reviews some of the existing literature on the subject of cryo-EM denoising. Sections 4 and 5 describe the construction of the polar transformer and some of its properties. Finally, Section 6 gives details of concrete models and how we trained and tested them.

2 Problem setup

The denoising problem in cryo-EM aims at recovering a clean image $x \in X$ from a noisy version $y \in X$. We represent all images through their pixel values on an $L \times L$ raster, i.e., $X = \mathbb{R}^{L \times L}$.

The clean images are assumed to be tomographic projections of a 3D potential density from a biological macromolecule. These are calculated using line integrals of that density along some chosen viewing direction. Following this, the images are filtered using a contrast transfer function (CTF) to simulate the optical properties of the microscope, and shifted randomly. We assume that these are individual particle projections (i.e., we are past the particle-picking stage). While simple, the above model has proven to be relatively accurate (Frank, 1996; Vulović et al., 2013) and is used in a range of cryo-EM reconstruction methods (Barnett et al., 2017; Scheres, 2012; Punjani et al., 2017; Zhong et al., 2021). To simulate the noisy projections y from the clean image x , we then use additive Gaussian noise, a common assumption in many reconstruction methods (Punjani et al., 2017).

We will now consider three distinct denoising tasks.

Single images The simplest setting is to consider each projection separately, potentially combining it with information from other projections later on. We thus have a mapping $f : X \rightarrow X$ such that $x \approx f(y)$. We call this the *single-image denoising task*. This is the setting of Wiener filters, which are trained on a large set of images and then applied separately to each noisy image.

One desirable property of f is equivariance to 2D rotations. This follows from the fact that the probability distribution of the images (both clean and noisy) is invariant to in-plane rotations (one image is as likely to appear in the data as a rotated copy of that image). Letting $R_\gamma : X \rightarrow X$ denote

the in-plane rotation of an image by $\gamma \in [0, 2\pi)$, we thus require

$$f(R_\gamma x) = R_\gamma(f(x)). \quad (1)$$

Directional sets More potent processing is possible when using a *set* of K images, $x \in X^K$, representing a selection of projections picked from a microscopy sample. In particular, we shall assume that these images all come from the same viewing direction and that they only differ by in-plane rotation (in other words, for each i, j , there is γ_{ij} such that $x_i = R_{\gamma_{ij}} x_j$). We call this the *directional set denoising task*. This situation arises, for example, during class averaging (see below) when the clustered images are to be aligned and averaged.

For this task, we extend the equivariance requirement it so that each image in the set is rotated by a different angle. In other words, we have the mapping $R_\gamma : X^K \rightarrow X^K$ for $\gamma \in [0, 2\pi]^K$ such that $(R_\gamma x)_i = R_{\gamma_i} x_i$. The equivariance relation in this case is

$$f(R_\gamma x) = R_\gamma(f(x)). \quad (2)$$

General sets In the general case, we cannot assume that our images have already been clustered by viewing direction. Instead, we rely on the fact that any sufficiently large set already contains such clusters of images that are the same up to rotation. This is the underlying idea of class averaging and represents the most typical denoising setting. We will refer to this as the *general set denoising task*. The challenge here is to identify the similar images in the set (up to rotation) and denoise them jointly. Again, the denoiser takes the form $f : X^K \rightarrow X^K$ and satisfies the equivariance property (equation 2), but we do not require that clean images are the same up to rotation.

3 Related work

Existing approaches to image denoising can be categorized into shallow (non-neural) approaches and DNNs. While the former often rely on geometrical properties of the images (Dabov et al., 2007), they also exploit (often implicitly) some prior knowledge about those images. DNNs have typically extended these methods by enriching the latter component, encoding stronger priors by training on a large set of images. They are however often less able to exploit geometrical properties.

Amongst the shallow denoising methods, the simplest is the filter. These can either be fixed low-pass filters (referred to as “binning”) (Barteseaghi et al., 2018), stationary Wiener filters (Frank et al., 1996; Tang et al., 2007; Sindelar & Grigorieff, 2011) or generalized Wiener filters calculated in a steerable basis Bhamre et al. (2016). While these have achieved a certain degree of success, they are fundamentally limited in that they are *linear* denoisers, and can therefore only achieve optimality with respect to a Gaussian prior distribution (Kay, 1993). Since the prior distribution of clean cryo-EM images is necessarily non-Gaussian, these methods result in clean, but overly blurred images.

Another method for denoising in cryo-EM is class averaging (van Heel, 1984; Park & Chirikjian, 2014; Zhao & Singer, 2014a; Scheres, 2015). The central idea here is to use the fact that all the images in a cryo-EM dataset cluster naturally by viewing direction. Indeed, given a particular projection image, it is often possible to find another set of images taken from the same viewing direction, but subject to a different in-plane rotation. The goal of class averaging methods is thus to classify (cluster) the images, align them, and then average. This results in less blurring compared to filter-based methods, but many (hundreds) images are needed to achieve a low error. Furthermore, the classification and alignment steps are sensitive to noise and therefore fail at low SNR.

Another means of improving denoisers is making them non-linear. An example is the DnCNN architecture (Zhang et al., 2017): a standard residual CNN trained to recreate the clean image from a noisy version of that image. While the work focused on denoising of photos, the technique can be applied to any set of images. Another architecture are U-Nets (Ronneberger et al., 2015; Gurrola-Ramos et al., 2021). In the context of cryo-EM images, these have been used for denoising, but only on entire micrographs (Bepko et al., 2020; Palovcak et al., 2020). Though this has the advantage over our approach of not requiring particle picking beforehand, it requires the network to learn any redundancy between the particles in the micrograph during training. The approach is also limited to exploiting the redundancy within a single micrograph, as opposed to over the whole dataset.

More generally, DNNs have been used in the cryo-EM reconstruction pipeline to provide stronger priors on the 3D reconstruction. For example, Kimanius et al. (2021, 2024) replaced the weak

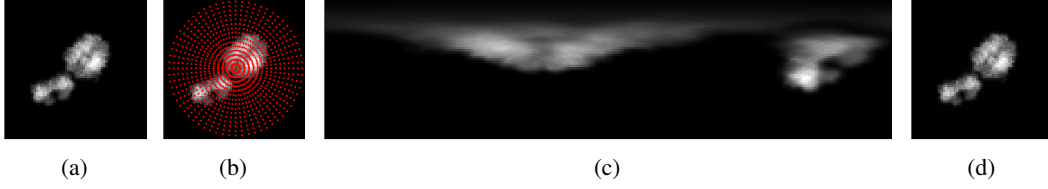


Figure 1: (a) A simulated 64×64 projection image of PDB ID 2pkq. (b) The projection image with a polar grid superimposed (downsampled by $4 \times$ for visualization). (c) The polar representation (horizontal axis: angles; vertical axis: radii). (d) The reconstructed image with RMSE $3.5 \cdot 10^{-4}$.

stationary Gaussian process used in the RELION (Scheres, 2012) software with a learned prior. This resulted in an increase in accuracy, but also showed signs of hallucination.

In a separate use case, DNNs have found widespread use in cryo-EM as a general-purpose function approximation tool. Here, DNNs are used in an unsupervised manner and optimized to a particular cryo-EM dataset, for example with the goal of fitting a 3D model (Zhong et al., 2021; Gupta et al., 2021; Schwab et al., 2024; Nashed et al., 2021; Levy et al., 2022) or the set of 2D projections (Bibas et al., 2021; Kwon et al., 2023; Nasiri & Bepler, 2022). Consequently, the neural networks typically do not impose a specific prior on the reconstructions beyond the inductive bias provided by the particular architecture. This is in contrast with the context of the present work and the approach of Bepler et al. (2020); Kimanius et al. (2021, 2024), where DNNs are trained to form universal estimators by encoding prior information extracted from publicly available datasets.

4 Polar decomposition and CNNs

For the task of denoising images, a natural approach is to train a convolutional neural network for the purpose, with noisy images as input and clean images as targets (Zhang et al., 2017; Gurrola-Ramos et al., 2021). While these have been successful in various domains, such as natural and medical images, they do not apply directly to cryo-EM projection images. The main reason is that a single cryo-EM image has a much higher level of noise compared to other modalities. We thus need to denoise multiple images *jointly* by classifying, aligning, and averaging them in the manner of class averaging (van Heel, 1984; Park & Chirikjian, 2014; Zhao & Singer, 2014a; Scheres, 2015). To achieve this using a neural network architecture, we need a representation that allows rotating images in an efficient and stable way. As it turns out, this will also enforce rotational equivariance, which is desirable in a cryo-EM denoiser due to the rotationally invariant distribution of images.

4.1 Polar representation

To achieve the properties discussed above, we propose decomposing the images via a weighed polar representation. The original images are given in the Cartesian domain, with pixels on an $L \times L$ grid; we map those images to a polar grid formed as the tensor product of radial and angular grids.

First, let us assume that the pixel size of the images corresponds to $2/L$, so that the $L \times L$ Cartesian grid spans the square $[-1, 1]^2$ (see Figure 1a). We now want to inscribe an $N \times M$ polar grid inside this square. The radii r_0, r_1, \dots, r_{N-1} are given by a Gauss–Jacobi quadrature rule over $[0, \sqrt{2} + \Delta]$ with parameters $(0, 1)$ (Ralston & Rabinowitz, 2001, Chapter 4.8–1) for some $\Delta \geq 0$. We denote the corresponding quadrature weights by w_0, w_1, \dots, w_{N-1} . The angles are given by $\gamma_m = 2\pi m/M$ for $m = 0, 1, \dots, M-1$. The resulting grid $\{(u_{nm}, v_{nm})\}_{nm}$ is then given by (see Figure 1b)

$$u_{nm} = r_n \cos \gamma_m \quad v_{nm} = r_n \sin \gamma_m. \quad (3)$$

Typically, N and M are chosen to be L and $4L$, respectively, while Δ can be $1/L$.

To map our Cartesian images with pixel values $x[i, j]$ to the polar domain, we place a Gaussian radial basis function (RBF) at each of the grid points and compute inner products. Let us assume that L is even and that the Cartesian image x is indexed by $-L/2, \dots, L/2 - 1$ along both axes.

The polar decomposition is then (see Figure 1c)

$$Px[n, m] = \frac{\sqrt{w_n}}{Z} \sum_{i,j=-L/2}^{L/2-1} x[i, j] e^{-\frac{(u_{nm}-2i/L)^2 + (v_{nm}-2j/L)^2}{2b^2}} \quad (4)$$

for $n = 0, 1, \dots, N-1$ and $m = 0, 1, \dots, M-1$, where b is a bandwidth factor typically set to $1/L$ and the normalization factor Z is given by $Z = \sqrt{2\pi^3 ML^2 b^4}$.

This representation enjoys a number of useful properties. For one, the original image can be provably recovered to arbitrary accuracy by an appropriate choice of parameters N , M , Δ and b (see Figure 1d and Appendix A). The representation is also an approximate isometry when restricted to smooth images (see Appendix B). Because of this, the polar mapping will not significantly distort the geometry of the original data manifold.

The mapping also enjoys stability in the sense that the operator norm $\|P\|$ can be shown to be approximately one (see Appendix B). In other words, small changes in x result in small changes in Px . This is in contrast with other polar representations, such as those obtained by nearest-neighbor or linear interpolation, which can introduce artifacts for small changes in the Cartesian image. This lack of artifacts simplifies the training of neural networks in the representation, improves their equivariance properties, and increases their robustness to noise. Finally, both P and its inverse can be applied efficiently, with computational complexity $\mathcal{O}(L^2)$ and $\mathcal{O}(L^2 \log L)$, respectively (see Appendix C).

4.2 Polar CNNs

A crucial property of the polar representation is that it commutes with rotation. Indeed, we have the relationship $PR_{\gamma_\ell} \approx S_\ell P$, where S_ℓ denotes circular shift along the second axis by ℓ and we recall that $\gamma_\ell = 2\pi\ell/M$. Rotation in the Cartesian domain thus corresponds to translation along the angular axis in the polar domain. Due to the stability of the polar mapping P , off-grid rotations will give sensible polar representations in the form of sub-grid shifts.

Equivariance to rotations in the Cartesian domain can therefore be achieved by equivariance to angular translations in the polar domain. The space of linear operators equivariant to such translations is spanned by *angular convolutions*: operators of the form

$$z \otimes h[n, m] = \sum_{p=0}^{N-1} \sum_{q=-Q}^Q z[p, m-q] h[n, p, q], \quad (5)$$

where z is a polar representation of size $N \times M$ and Q is the (angular) width of h (typically in the range 1–3). We refer to h as an *angular filter*, with two radial indices n, p and one angular index q .

Note that the operation above only convolves along the angular axis. Along the radial axis, it amounts to a matrix multiplication (i.e., a fully connected layer). We can enforce localization of the filter along the radial axis by restricting its support. Specifically, we set $h[n, p, q] = 0$ whenever $|n - p| > W$, for some radial width W (typically in the range 1–3).

The angular filter can be trivially generalized to multiple channels and be used as a linear layer in a DNN. Since the polar representation is essentially a reparametrization of the original Cartesian image, standard layers from CNNs can be applied to the output of the angular convolutions, such as ReLUs (Goodfellow et al., 2016), avoiding less natural spectral non-linearities required for other equivariant networks (Kondor et al., 2018). The above construction also avoids costly transformations between an equivariant basis and a natural image basis (Cohen et al., 2018). Finally, we note that this also be formulated as an $\text{SO}(2)$ -CNN in the formalism of Kondor & Trivedi (2018).

We shall refer to a DNN consisting of the angular convolutions described above as *polar CNNs*.

5 Polar transformer

Going beyond single-image denoising requires a way to combine information from multiple images. In the cryo-EM setting, copies of the same molecule are imaged from different directions, forming the basis for the common denoising methods of class averaging.

One direct extension would be to apply a class averaging method to denoised images. However, this may result in inferior results, as a single-image denoiser may potentially discard information relevant to clustering and alignment. We will instead combine denoising and class averaging into an end-to-end network that learns how to optimally cluster and align the images.

A natural architecture for aggregating disparate sources of information is the transformer, originally introduced in the field of language models (Vaswani et al., 2017; Devlin et al., 2018; Brown et al., 2020). Here, a sequence of *tokens* is used to generate key, query, and value vectors that are combined using what is known as an *attention mechanism* (Vaswani et al., 2017). In language models, tokens are parts of words, but they can be any information carrier, such as an image.

Let us consider a multi-channel polar image $z[c, n, m]$, where $c = 0, 1, \dots, C - 1$ is the channel index, $n = 0, 1, \dots, N - 1$ is the radial index, and $m = 0, 1, \dots, M - 1$ is the angular index. These are used as input to three polar CNNs, denoted f_θ^{key} , f_θ^{query} , and f_θ^{value} , corresponding to the key, query, and value networks, respectively. Here, θ is a shared weights vector.

While the standard attention mechanism may be useful for combining information in the images by clustering them appropriately, it has two important drawbacks: it cannot align the images rotationally and it is not equivariant to rotations. In fact, it turns out that these problems are closely related – an attention mechanism that is rotationally equivariant must also perform alignment.

Now suppose we have a set $\mathbf{z} = (z_0, z_1, \dots, z_{K-1})$ of K multi-channel polar images, which we process using the above networks to obtain key, query, and value vectors. To see how this can be achieved, let us consider an augmented form of the standard attention mechanism, where each key is rotated by an arbitrary angle γ_ℓ , that is, shifted by ℓ along the angular axis. We then have a set of rotated attention coefficients given by

$$\alpha_{k,k'}^{(\ell)}(\mathbf{z}) = \sigma \left(\frac{1}{\sqrt{CNM}} \sum_{c,n,m} f_\theta^{\text{query}}(z_k)[c, n, m] S_\ell f_\theta^{\text{key}}(z_{k'})[c, n, m] \right), \quad (6)$$

for $\ell = 0, 1, \dots, M - 1$, where the softmax σ is taken over indices k' and ℓ . We then apply a corresponding rotation to the value vectors when performing the linear combination, to obtain

$$(f_\theta^{\text{ang-attention}}(\mathbf{z}))_k = \sum_{\ell=0}^{M-1} \sum_{k'=0}^{K-1} \alpha_{k,k'}^{(\ell)}(\mathbf{z}) S_\ell f_\theta^{\text{value}}(z_{k'}) \quad (7)$$

for $k = 0, 1, \dots, K - 1$. While this would seem to incur a significant computational expense, the augmented attention coefficients and the output images can be calculated by convolution along the angular axis. This allows efficient implementation using fast Fourier transforms (FFTs).

Since it performs attention along the angular axis, we refer to this as the *angular attention mechanism*. It gives the network the ability to align images rotationally and combine them accordingly. It also satisfies an extended equivariance property. Let S_ℓ denote the joint angular shifting operator for K images by $\ell \in \mathbb{Z}^K$ such that $(S_\ell \mathbf{z})_k = S_{\ell_k} z_k$. It can then be shown that

$$f_\theta^{\text{ang-attention}}(S_\ell \mathbf{z}) = S_\ell f_\theta^{\text{ang-attention}}(\mathbf{z}). \quad (8)$$

In the Cartesian domain, this means that we have joint equivariance to rotation of the individual images in the set, i.e., the network is $\text{SO}(2)^K$ -equivariant. As a result, a denoiser based on this mechanism satisfies the desired equivariance property for sets of projection images (see equation 2).

By stacking one or multiple angular attention blocks together with polar CNNs for pre- and post-processing, we obtain a *polar transformer*.

6 Experiments and results

To evaluate the architectures proposed above, we conduct numerical experiments on simulated data. These show how the polar CNN and polar transformer are able to achieve very low denoising errors despite high noise levels, significantly outperforming baseline methods.

6.1 Neural networks

Two neural network architectures are used in the experiments. The first is a simple polar CNN consisting of a Cartesian-to-polar layer, 25 angular convolutional layers with $C = 8$ channels each, each

followed by a GroupNorm layer (with 4 groups) (Wu & He, 2018) and a ReLU nonlinearity (Goodfellow et al., 2016). Finally, the polar representation was converted back to the Cartesian domain. The convolutional layers had an angular kernel width of $Q = 5$ and a radial kernel width of $W = 5$.

The other network is a polar transformer, starting with a Cartesian-to-polar layer followed by a polar CNN preprocessing network of depth 5 applied individually to each image in the set. This was followed by an angular attention module where the key and query networks consisted of the same polar CNN of depth 17 with shared weights (the value network was the identity). Finally, the attention output was postprocessed in a 9-layer polar CNN before conversion to Cartesian. The convolutional layers in the CNNs had the same configuration for the polar CNN, but the pre- and post-processing networks had $C = 8$ while the key- and query-network had $C = 16$.

6.2 Data

Both architectures were trained on simulated data obtained from 5 000 molecular structures downloaded from the PDB (wwPDB consortium, 2018). Each molecule is projected through 1 000 different viewing directions yielding a total of 5 000 000 clean projection images. The same process was used for another 100 molecules, resulting in a testing set of 500 000 clean images. Both of these were then split in three different datasets for training and testing.

In the directional set denoising task, each clean image was then rotated randomly, resulting in $K = 8$ different clean images. For general set denoising, two clean images from one molecule corresponding to two different viewing directions were picked, each rotated to yield 8 copies, yielding a total of $2K = 16$ images. In both cases, the whole image set was used as input to the transformer model.

For all denoising tasks, we consider three different noise configurations: additive Gaussian noise, additive Gaussian noise plus shifts and CTF, and Poisson noise. In the first case, a Gaussian white noise realization is added to the clean images to achieve the desired SNR. In the second, we apply a CTF of random defocus (between 15000 Å and 25000 Å) and a random shift (of maximum 8 pixels) before adding the Gaussian noise. For details on the Poisson case, see Appendix G.

6.3 Training and testing procedures

Each model was trained using the training sets described above for a specific SNR (the average square magnitude of the clean images divided by the noise variance). The models can also be trained to generalize over a range of SNRs, but we present results for fixed-SNR models here for simplicity. The DnCNN model follows Zhang et al. (2017), but with the residual connection removed. The U-Net is the one used in the Topaz pipeline (Bepler et al., 2020), with added group normalization (with 4 groups) to avoid explosion of weights at low SNR.

All architectures were trained to minimize mean squared error loss using the Adam optimizer (Kingma & Ba, 2017) at learning rate 10^{-3} and batch size 128. Convergence was typically obtained after ten epochs for all models. Training time per epoch was around 1.3 hours (polar CNN and U-Net), 1.8 hours (DnCNN), and 12.5 hours (polar transformer) on an A100 GPU.

6.4 Denoising results

We first consider the additive white Gaussian noise configuration (i.e., no CTF or shifts). Figure 2a shows that the polar CNN network outperforms the other single-image denoisers (the DnCNN and U-Net) which do not explicitly encode rotational equivariance (and therefore perform slightly worse) but learn it through the data augmentation implicit in the training data. Going beyond the polar CNN, we see that the polar transformer model consistently outperform single-image methods when given a directional image set (i.e., the underlying clean images are the same up to in-plane rotation). In particular, we see an reduction of relative mean squared error (MSE) from 0.10 (DnCNN and U-Net) to 0.055 (polar transformer) at $\text{SNR} = 0.03$, a reduction of 45%. By studying the attention coefficients, we can also verify that the transformer is able to correctly recover the rotation angle in a robust manner (see Appendix D).

Finally, we see that the polar transformer is also able to cluster sets of noisy images in the general set denoising task. While performance is strictly worse, it remains quite close to the directional set results, with a 10% increase in relative MSE at $\text{SNR} = 0.03$ and still well ahead of the baseline

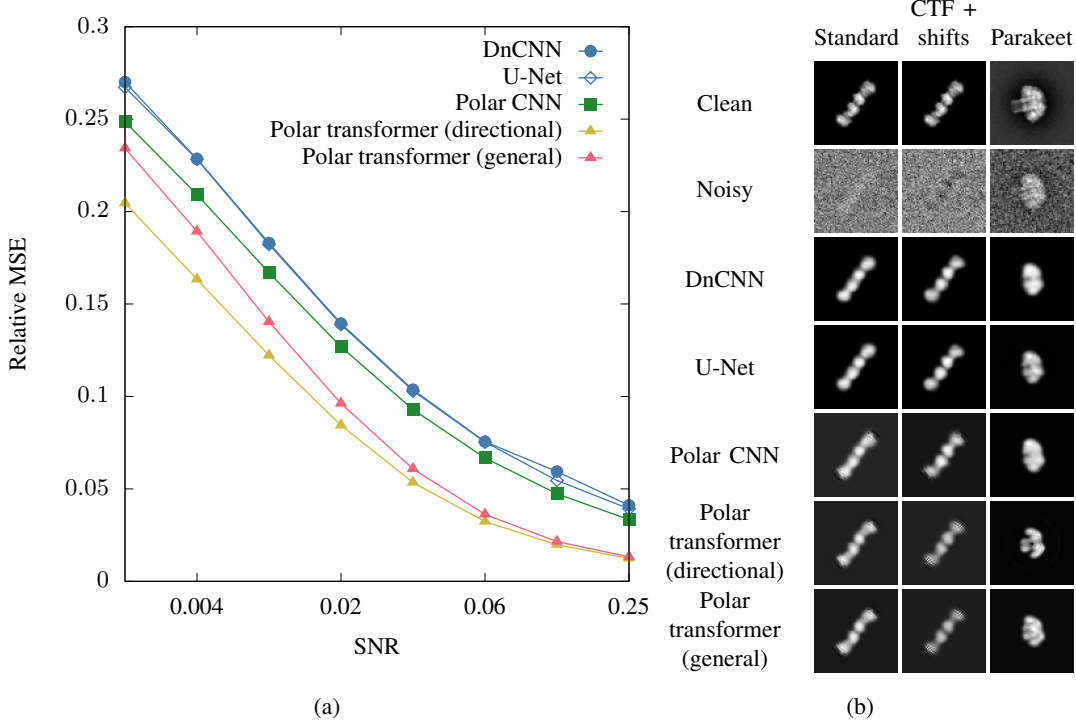


Figure 2: (a) The denoising MSE for SNRs of Gaussian noise. The DnCNN, U-Net, and polar CNN models denoise individual images, while the transformers denoise sets of images (the directional set contains eight images while the general set contains sixteen images split evenly over two viewing directions). (b) Sample images for the standard configuration at $\text{SNR} = 0.03$ (first column), with CTF and shifts at $\text{SNR} = 0.02$ (second column), and for the Parakeet simulator (third column).

methods. Looking at the activation coefficients of the attention module (see Appendix E), we see that these indeed cluster the different viewing directions as expected. We also see in the example images of Figure 2b (first column) how the polar CNN produces of comparable quality to that of DnCNN and U-Net, but that the polar transformer produces sharper, higher-quality images.

Recall that these results are for an additive Gaussian white noise model. By incorporating CTFs and shifts, we obtain a more realistic forward model. Retraining the same models on a training set with $\text{SNR} = 0.02$, we relative MSEs of 0.089 for the U-Net, 0.088 for the DnCNN, 0.081 for the polar CNN, and 0.042 for the polar transformer on directional sets and 0.049 for the polar transformer on the general sets. Again, the polar CNN performs similarly to the conventional single-image denoisers (DnCNN and U-Net), while the polar transformer offers a significant reduction in error (see Figure 2b, second column). One important advantage of the latter is that it can recover information lost due to CTF-filtering since each image in the set has a different CTF applied to it, allowing the network to recover the missing information by combining multiple images. More examples of denoised images can be found in Appendix F.

Finally, we see that the models are not very sensitive to the noise distribution: models trained on Gaussian noise can also be applied successfully to images subjected to Poisson noise (see Appendix G). There is a small loss in MSE, but the overall features are preserved.

Although the forward model used in the above experiments incorporates the main aspects of the cryo-EM imaging process, it is a somewhat crude approximation. To assess qualitatively how far the current models are from being usable with true micrographs, we applied them also to some projections generated with the Parakeet digital twin Parkhurst et al. (2021), which uses multislice simulations to produce more accurate synthetic images. We used Parakeet to generate a “clean” projection (by taking a very high electron dose) and a noisy one to which the single-image denoisers (DnCNN, U-Net, and polar CNN) were applied. Each was able to recover the clean image well, but all suffered some loss of detail (see Figure 2b, third column).

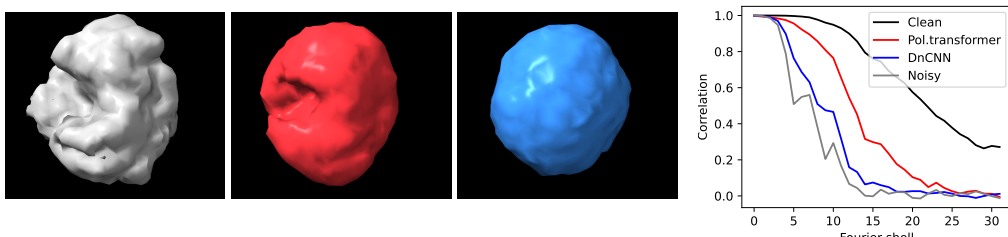


Figure 3: (left) 3D reconstructions of dmso reductase from denoised images: ground truth (gray), polar transformer (red), and DnCNN (blue). (right) FSC curves of the reconstructions.

To evaluate the effect of the polar transformer, we generated an additional set of 10 000 projections and picked two sets of images of similar viewing direction (within ten degrees, but with arbitrary in-plane rotation). The first set, containing eight images, was given to the polar transformer trained on directional sets, while another, containing sixteen images, was given to the one trained on general sets. We used Parakeet to generate a dataset of 10 000 projections, from which a set of eight images were extracted that had similar projection directions (within ten degrees). This was sufficient to yield improved results compared to the single-image denoisers (see Figure 2b, third column).

6.5 3D reconstruction

While there is a value in denoising projection images themselves, the ultimate goal of cryo-EM processing is to construct a 3D model of the imaged molecule. This is typically done in two steps: an initial, low-resolution reconstruction, known as an *ab initio* model, which is followed by high-resolution refinement. There are several algorithms for *ab initio* modeling, such as marginalized maximum a posteriori estimation (Punjani et al., 2017) or angular reconstitution (van Heel, 1987).

We will focus on a class of methods based on common lines (Singer & Shkolnisky, 2011), which relies on the intersection geometry of the projection images in Fourier space. As these methods are quite sensitive to noise, their performance can be significantly enhanced by denoising. To evaluate this, we generated 2048 noisy projection images of dmso reductase (PDB ID 1DMR) at $\text{SNR} = 0.25$ that we processed either using a DnCNN or the polar transformer (trained on directional sets). For the latter, we clustered the images into sets of 8 images each according to their viewing direction (up to in-plane rotation), mimicking the 2D classification step in the cryo-EM processing pipeline. These sets were then fed into the polar transformer model.

Both sets of denoised images were then used as input to the sync3n *ab initio* reconstruction algorithm implemented in the ASPIRE package Wright et al. (2025). Compared to the ground truth orientations, the DnCNN images achieved a mean angular distance of 111° , while the polar transformer achieved 69.7° . The resulting orientations were then paired with the original noisy images (to avoid bias induced by the denoising process) to obtain 3D reconstructions by inverting the forward model using the method of least squares. The results are shown in Figure 3. We see that the increased accuracy in orientation estimation achieved by the polar transformer results in more accurate 3D models. This is also reflected in the Fourier shell correlation (Harauz & van Heel, 1986) (see Figure), where the estimated orientations from the polar transformer better capture higher-resolution information in the 3D density map. For more reconstruction examples, see Appendix I.

7 Conclusion

In this work, we have presented a new powerful architecture for joint denoising of cryo-EM projection images: the polar transformer. While this model has significant potential, more work remains before it can be applied to practical problems. The most important of these involve scaling the model to larger datasets and unsupervised training on experimental data. While crucial to applying the proposed methods to real-world data, both of these tasks involve development of methods for training and evaluating the proposed model and are therefore fall outside the scope of the current work (see Appendix H). Nonetheless, we believe that the polar transformer provides an important first step in the direction of a fully end-to-end cryo-EM reconstruction pipeline.

Acknowledgments

The authors would like to thank Eftychios Pnevmatikakis, who worked on an earlier prototype of the above architecture and provided invaluable advice. Similarly, the authors would like to thank Olivier Verdier for his thoughtful comments in discussions of our approach and results. Further thanks to Axel Janson for generating the Parakeet test data. This work was funded by grants from the Göran Gustafsson Foundation and the Swedish Research Council through grant no. 2023-04143. The computations were enabled by resources provided by the National Academic Infrastructure for Supercomputing in Sweden (NAISS), partially funded by the Swedish Research Council through grant agreement no. 2022-06725. The Flatiron Institute is a division of the Simons Foundation.

References

- Barnett, A., Greengard, L., Pataki, A., and Spivak, M. Rapid solution of the cryo-EM reconstruction problem by frequency marching. *SIAM Journal on Imaging Sciences*, 10(3):1170–1195, 2017. doi: 10.1137/16M1097171.
- Barnett, A. H., Magland, J., and af Klinteberg, L. A parallel nonuniform fast Fourier transform library based on an “exponential of semicircle” kernel. *SIAM Journal on Scientific Computing*, 41(5):C479–C504, 2019. doi: 10.1137/18M120885X.
- Bartesaghi, A., Aguerrebere, C., Falconieri, V., Banerjee, S., Earl, L. A., Zhu, X., Grigorieff, N., Milne, J. L., Sapiro, G., Wu, X., and Subramaniam, S. Atomic resolution cryo-EM structure of β -galactosidase. *Structure*, 26(6):848–856.e3, Jun 2018. doi: 10.1016/j.str.2018.04.004.
- Bendory, T., Bartesaghi, A., and Singer, A. Single-particle cryo-electron microscopy: Mathematical theory, computational challenges, and opportunities. *IEEE Signal Processing Magazine*, 37(2): 58–76, mar 2020. doi: 10.1109/msp.2019.2957822.
- Bepler, T., Noble, A. J., and Berger, B. Topaz-denoise: general deep denoising models for cryoEM and cryoET. *Nature Communications*, 11(1), 2020. doi: 10.1038/s41467-020-18952-1.
- Bertero, M., Boccacci, P., and De Mol, C. *Introduction to Inverse Problems in Imaging*. 2 edition, 2021. doi: 10.1201/9781003032755.
- Bhamre, T., Zhang, T., and Singer, A. Denoising and covariance estimation of single particle cryo-EM images. *Journal of Structural Biology*, 195(1):72–81, jul 2016. ISSN 1047-8477. doi: 10.1016/j.jsb.2016.04.013.
- Bibas, K., Weiss-Dicker, G., Cohen, D., Cahan, N., and Greenspan, H. Learning rotation invariant features for cryogenic electron microscopy image reconstruction. In *Proc. ISBI*, pp. 563–566, 2021. doi: 10.1109/ISBI48211.2021.9433789.
- Brown, T. B., Mann, B., Ryder, N., Subbiah, M., Kaplan, J., Dhariwal, P., Neelakantan, A., Shyam, P., Sastry, G., Askell, A., Agarwal, S., Herbert-Voss, A., Krueger, G., Henighan, T., Child, R., Ramesh, A., Ziegler, D. M., Wu, J., Winter, C., Hesse, C., Chen, M., Sigler, E., Litwin, M., Gray, S., Chess, B., Clark, J., Berner, C., McCandlish, S., Radford, A., Sutskever, I., and Amodei, D. Language models are few-shot learners. 2020. URL <https://arxiv.org/abs/2005.14165>.
- Buchholz, T.-O., Jordan, M., Pigino, G., and Jug, F. Cryo-care: Content-aware image restoration for cryo-transmission electron microscopy data. In *2019 IEEE 16th International Symposium on Biomedical Imaging (ISBI 2019)*, pp. 502–506, 2019. doi: 10.1109/ISBI.2019.8759519.
- Cohen, T. S., Geiger, M., Köhler, J., and Welling, M. Spherical CNNs. In *International Conference on Learning Representations*, 2018.
- Dabov, K., Foi, A., Katkovnik, V., and Egiazarian, K. Image denoising by sparse 3-D transform-domain collaborative filtering. *IEEE Transactions on Image Processing*, 16(8):2080–2095, 2007. doi: 10.1109/TIP.2007.901238.
- Devlin, J., Chang, M.-W., Lee, K., and Toutanova, K. Bert: Pre-training of deep bidirectional transformers for language understanding. *arXiv preprint*, 2018.

- DLMF. *NIST Digital Library of Mathematical Functions*. URL <https://dlmf.nist.gov/>. F. W. J. Olver, A. B. Olde Daalhuis, D. W. Lozier, B. I. Schneider, R. F. Boisvert, C. W. Clark, B. R. Miller, B. V. Saunders, H. S. Cohl, and M. A. McClain, eds.
- Dubochet, J., Lepault, J., Freeman, R., Berriman, J. A., and Homo, J.-C. Electron microscopy of frozen water and aqueous solutions. *Journal of Microscopy*, 128(3):219–237, 1982. doi: 10.1111/j.1365-2818.1982.tb04625.x.
- Frank, J. *Three-Dimensional Electron Microscopy of Macromolecular Assemblies*. Academic Press, 1996.
- Frank, J., Radermacher, M., Penczek, P., Zhu, J., Li, Y., Ladjadj, M., and Leith, A. SPIDER and WEB: processing and visualization of images in 3D electron microscopy and related fields. *Journal of Structural Biology*, 116(1):190–199, 1996.
- Goodfellow, I., Bengio, Y., and Courville, A. *Deep learning*. MIT press, 2016.
- Greengard, L. and Lee, J.-Y. Accelerating the nonuniform fast Fourier transform. *SIAM Review*, 46(3):443–454, 2004. doi: 10.1137/S003614450343200X.
- Gupta, H., McCann, M. T., Donati, L., and Unser, M. CryoGAN: A new reconstruction paradigm for single-particle cryo-EM via deep adversarial learning. *IEEE Transactions on Computational Imaging*, 7:759–774, 2021.
- Gurrola-Ramos, J., Dalmau, O., and Alarcón, T. E. A residual dense u-net neural network for image denoising. *IEEE Access*, 9:31742–31754, 2021.
- Harauz, G. and van Heel, M. Exact filters for general geometry three dimensional reconstruction. *Optik*, 73(4):146–156, 1986.
- Iudin, A., Korir, P. K., Somasundharam, S., Weyand, S., Cattavittello, C., Fonseca, N., Salih, O., Kleywegt, G., and Patwardhan, A. EMPIAR: the electron microscopy public image archive. *Nucleic Acids Research*, 51(D1):D1503–D1511, 11 2022. ISSN 0305-1048. doi: 10.1093/nar/gkac1062.
- Jensen, G. J. Alignment error envelopes for single particle analysis. *Journal of Structural Biology*, 133(2):143–155, 2001. ISSN 1047-8477. doi: 10.1006/jsbi.2001.4334.
- Kay, S. M. *Fundamentals of Statistical Signal Processing: Estimation Theory*. Prentice Hall, 1993.
- Kimanius, D., Zickert, G., Nakane, T., Adler, J., Lunz, S., Schönlieb, C.-B., Öktem, O., and Scheres, S. H. Exploiting prior knowledge about biological macromolecules in cryo-EM structure determination. *IUCrJ*, 8:60–75, 2021. doi: 10.1101/2020.03.25.007914.
- Kimanius, D., Jamali, K., Wilkinson, M. E., Lövestam, S., Velazhahan, V., Nakane, T., and Scheres, S. H. Data-driven regularization lowers the size barrier of cryo-EM structure determination. *Nature Methods*, 21(7):1216–1221, Jul 2024. doi: 10.1038/s41592-024-02304-8.
- Kingma, D. P. and Ba, J. Adam: A method for stochastic optimization. *arXiv preprint*, 2017.
- Kondor, R. and Trivedi, S. On the generalization of equivariance and convolution in neural networks to the action of compact groups. In *Proceedings of the 35th International Conference on Machine Learning*, volume 80, pp. 2747–2755. PMLR, 10–15 Jul 2018.
- Kondor, R., Lin, Z., and Trivedi, S. Clebsch–Gordan nets: a fully Fourier space spherical convolutional neural network. In *Advances in Neural Information Processing Systems*, volume 31, 2018.
- Kwon, S., Choi, J. Y., and Ryu, E. K. Rotation and translation invariant representation learning with implicit neural representations. In *Proc. ICML*, volume 202, pp. 18037–18056. PMLR, 23–29 Jul 2023.
- Lehtinen, J., Munkberg, J., Hasselgren, J., Laine, S., Karras, T., Aittala, M., and Aila, T. Noise2Noise: Learning image restoration without clean data. In *Proc. ICML*, volume 80, pp. 2965–2974, 2018.

- Levy, A., Wetzstein, G., Martel, J. N., Poitevin, F., and Zhong, E. Amortized inference for heterogeneous reconstruction in cryo-EM. In *Proc. NeurIPS*, volume 35, pp. 13038–13049, 2022.
- Nashed, Y. S., Poitevin, F., Gupta, H., Woollard, G., Kagan, M., Yoon, C. H., and Ratner, D. CryoPoseNet: End-to-end simultaneous learning of single-particle orientation and 3D map reconstruction from cryo-electron microscopy data. In *Proc. ICCV*, pp. 4066–4076, 2021.
- Nasiri, A. and Bepler, T. Unsupervised object representation learning using translation and rotation group equivariant VAE. In *Proc. NeurIPS*, volume 35, pp. 15255–15267, 2022.
- Palovcak, E., Asarnow, D., Campbell, M. G., Yu, Z., and Cheng, Y. Enhancing the signal-to-noise ratio and generating contrast for cryo-EM images with convolutional neural networks. *IUCrJ*, 7(6):1142–1150, Nov 2020. doi: 10.1107/S2052252520013184.
- Park, W. and Chirikjian, G. S. An assembly automation approach to alignment of noncircular projections in electron microscopy. *IEEE Transactions on Automation Science and Engineering*, 11(3):668–679, 2014. doi: 10.1109/TASE.2013.2295398.
- Parkhurst, J. M., Dumoux, M., Basham, M., Clare, D., Siebert, C. A., Varslot, T., Kirkland, A., Naismith, J. H., and Evans, G. Parakeet: a digital twin software pipeline to assess the impact of experimental parameters on tomographic reconstructions for cryo-electron tomography. *Open Biology*, 11(10):210160, 2021. doi: 10.1098/rsob.210160.
- Punjani, A., Rubinstein, J. L., Fleet, D. J., and Brubaker, M. A. cryoSPARC: algorithms for rapid unsupervised cryo-EM structure determination. *Nature Methods*, 14(3):290–296, 2017. doi: 10.1038/nmeth.4169.
- Ralston, A. and Rabinowitz, P. *A first course in numerical analysis*. Courier Corporation, 2001.
- Ronneberger, O., Fischer, P., and Brox, T. U-net: Convolutional networks for biomedical image segmentation. In *MICCAI 2015*, pp. 234–241. Springer, 2015.
- Sanchez-Garcia, R., Gomez-Blanco, J., Cuervo, A., Carazo, J. M., Sorzano, C. O. S., and Vargas, J. DeepEMhancer: a deep learning solution for cryo-EM volume post-processing. *Communications Biology*, 4(1):874, Jul 2021. doi: 10.1038/s42003-021-02399-1.
- Scheres, S. H. RELION: Implementation of a Bayesian approach to cryo-EM structure determination. *Journal of Structural Biology*, 180(3):519–530, 2012. ISSN 1047-8477. doi: 10.1016/j.jsb.2012.09.006.
- Scheres, S. H. Semi-automated selection of cryo-EM particles in RELION-1.3. *Journal of Structural Biology*, 189(2):114–122, 2015. ISSN 1047-8477. doi: 10.1016/j.jsb.2014.11.010.
- Schwab, J., Kimanius, D., Burt, A., Dendooven, T., and Scheres, S. H. DynaMight: estimating molecular motions with improved reconstruction from cryo-EM images. *Nature Methods*, pp. 1–8, 2024.
- Shih, Y.-h., Wright, G., Andén, J., Blaschke, J., and Barnett, A. H. cuFINUFFT: a load-balanced GPU library for general-purpose nonuniform FFTs. In *2021 IEEE International Parallel and Distributed Processing Symposium Workshops (IPDPSW)*, pp. 688–697, 2021. doi: 10.1109/IPDPSW52791.2021.00105.
- Sindelar, C. V. and Grigorieff, N. An adaptation of the Wiener filter suitable for analyzing images of isolated single particles. *Journal of structural biology*, 176(1):60–74, 2011.
- Singer, A. and Shkolnisky, Y. Three-dimensional structure determination from common lines in Cryo-EM by eigenvectors and semidefinite programming. *SIAM Journal on Imaging Sciences*, 4(2):543–572, 2011. doi: 10.1137/090767777.
- Singer, A. and Sigworth, F. J. Computational methods for single-particle electron cryomicroscopy. *Annual Review of Biomedical Data Science*, 3(Volume 3, 2020):163–190, 2020. doi: 10.1146/annurev-biodatasci-021020-093826.
- Stein, E. M. and Weiss, G. *Introduction to Fourier Analysis on Euclidean Spaces*. Princeton University Press, 1971. ISBN 978-0-691-08078-9.

- Tang, G., Peng, L., Baldwin, P. R., Mann, D. S., Jiang, W., Rees, I., and Ludtke, S. J. EMAN2: An extensible image processing suite for electron microscopy. *Journal of Structural Biology*, 157(1): 38–46, 2007. ISSN 1047-8477. doi: 10.1016/j.jsb.2006.05.009. Software tools for macromolecular microscopy.
- van Heel, M. Multivariate statistical classification of noisy images (randomly oriented biological macromolecules). *Ultramicroscopy*, 13(1–2):165–183, jan 1984. doi: 10.1016/0304-3991(84)90066-4.
- van Heel, M. Angular reconstitution: a posteriori assignment of projection directions for 3D reconstruction. *Ultramicroscopy*, 21(2):111–123, 1987.
- Vaswani, A., Shazeer, N., Parmar, N., Uszkoreit, J., Jones, L., Gomez, A. N., Kaiser, L., and Polosukhin, I. Attention is all you need. In *Proc. NeurIPS*, volume 30, 2017.
- Vulović, M., Ravelli, R. B., van Vliet, L. J., Koster, A. J., Lazić, I., Lücken, U., Rullgård, H., Öktem, O., and Rieger, B. Image formation modeling in cryo-electron microscopy. *Journal of Structural Biology*, 183(1):19–32, 2013. doi: 10.1016/j.jsb.2013.05.008.
- Wagner, T., Merino, F., Stabrin, M., Moriya, T., Antoni, C., Apelbaum, A., Hagel, P., Sitsel, O., Raisch, T., Prumbaum, D., Quentin, D., Roderer, D., Tacke, S., Siebolds, B., Schubert, E., Shaikh, T. R., Lill, P., Gatsogiannis, C., and Raunser, S. SPHIRE-crYOLO is a fast and accurate fully automated particle picker for cryo-EM. *Communications Biology*, 2(1):218, Jun 2019. doi: 10.1038/s42003-019-0437-z.
- Wang, F., Gong, H., Liu, G., Li, M., Yan, C., Xia, T., Li, X., and Zeng, J. DeepPicker: A deep learning approach for fully automated particle picking in cryo-EM. *Journal of Structural Biology*, 195(3):325–336, 2016. ISSN 1047-8477. doi: 10.1016/j.jsb.2016.07.006.
- Wright, G., Andén, J., Bansal, V., Xia, J., Langfield, C., Carmichael, J., Sowattanangkul, K., Brook, R., Shi, Y., Heimowitz, A., Pragier, G., Sason, I., Moscovich, A., Shkolnisky, Y., and Singer, A. Computationalcryoem/aspire-python: v0.13.2, 2025. URL <https://zenodo.org/doi/10.5281/zenodo.5657281>.
- Wu, Y. and He, K. Group normalization. In *Proc. ECCV*, pp. 3–19, 2018.
- wwPDB consortium. Protein data bank: the single global archive for 3D macromolecular structure data. *Nucleic Acids Research*, 47(D1):D520–D528, oct 2018. ISSN 1362-4962. doi: 10.1093/nar/gky949.
- Zhang, K., Zuo, W., Chen, Y., Meng, D., and Zhang, L. Beyond a Gaussian denoiser: Residual learning of deep CNN for image denoising. *IEEE Transactions on Image Processing*, 26(7): 3142–3155, 2017.
- Zhao, Z. and Singer, A. Rotationally invariant image representation for viewing direction classification in cryo-EM. *Journal of Structural Biology*, 186(1):153–166, 2014a. ISSN 1047-8477. doi: 10.1016/j.jsb.2014.03.003.
- Zhao, Z. and Singer, A. Rotationally invariant image representation for viewing direction classification in cryo-EM. *Journal of Structural Biology*, 186(1):153–166, 2014b. ISSN 1047-8477. doi: 10.1016/j.jsb.2014.03.003.
- Zhong, E. D., Bepko, T., Berger, B., and Davis, J. H. CryoDRGN: reconstruction of heterogeneous cryo-EM structures using neural networks. *Nature Methods*, 18(2):176–185, 2021.

A Inverting the polar representation

Applying the adjoint of equation 4 to some polar image $z[n, m]$ gives back a Cartesian image $P^T z[i, j]$. This does not recover the original image x , but the following proposition shows that it can be approximated as a convolution for N and M large enough.

Proposition 1. *Let*

$$\phi[i, j] = \frac{1}{\pi b^2 L^2} \exp\left(-\frac{i^2 + j^2}{b^2 L^2}\right). \quad (9)$$

Then

$$P^T P x[i, j] = x \star \phi[i, j] + \varepsilon, \quad (10)$$

where \star denotes a discrete 2D convolution and

$$\varepsilon = O\left(\frac{(\sqrt{2} + \Delta)^2}{N^2 b^4} + \left(\frac{M!}{2M!}\right)^2 \left(\frac{2}{b^2}\right)^M + b e^{-\Delta^2/b^2}\right). \quad (11)$$

Proof. To see why $P^T P$ can be approximated with a discrete convolution, let us write out the full expression

$$\begin{aligned} P^T P x[p, q] &= Z^{-2} \sum_{n=0}^{N-1} w_n \sum_{m=0}^{M-1} e^{-\frac{(u_{nm}-2p)^2 + (v_{nm}-2q)^2}{2b^2}} \\ &\quad \sum_{i,j=-L/2}^{L/2-1} x[i, j] e^{-\frac{(u_{nm}-2i/L)^2 + (v_{nm}-2j/L)^2}{2b^2}} \end{aligned} \quad (12)$$

$$\begin{aligned} &= Z^{-2} \sum_{i,j=-L/2}^{L/2-1} 2\pi M e^{-\frac{(2i/L-2p/L)^2 + (2j/L-2q/L)^2}{4b^2}} x[i, j] \\ &\quad \sum_{n=0}^{N-1} \sum_{m=0}^{M-1} \frac{w_n}{2\pi M} e^{-\frac{((i+p)/L-u_{nm})^2 + ((j+q)/L-v_{nm})^2}{b^2}}, \end{aligned} \quad (13)$$

where we have used the identity

$$(a-c)^2 + (b-c)^2 = \frac{1}{2}(a-b)^2 + 2\left(\frac{a+b}{2} - c\right)^2. \quad (14)$$

We now set $x = (i+p)/L$ and $y = (j+q)/L$ and note that $(x, y) \in [-1, 1]^2$. Recall that we have $u_{nm} = r_n \cos(\alpha_m)$ and $v_{nm} = r_n \sin(\alpha_m)$ as described in equation 3. The sum over n and m above can therefore be written as

$$\sum_{n=0}^{N-1} \sum_{m=0}^{M-1} \frac{w_n}{2\pi M} e^{-\frac{(x-r_n \cos(\alpha_m))^2 + (y-r_n \sin(\alpha_m))^2}{b^2}}. \quad (15)$$

We first consider the sum over the angular index m for a fixed n . This is a sum of the periodic function $s_n(\alpha) = e^{-\frac{(x-r_n \cos(\alpha))^2 + (y-r_n \sin(\alpha))^2}{b^2}}$ sampled on a uniform grid over $[0, 2\pi)$ of size M . Using a Fourier series decomposition of $s_n(\alpha)$, we can see that this sum is equal to

$$\int_0^{2\pi} s_n(\alpha) d\alpha + \epsilon, \quad (16)$$

where $|\epsilon| \leq \frac{C}{N^2} \int_0^{2\pi} |s_n''(\alpha)| d\alpha$ for some constant C . Differentiating $s_n(\alpha)$ and using the fact that $r_n < \sqrt{2} + \Delta$, we have that $|s_n''(\alpha)| \leq C(\sqrt{2} + \Delta)r_n$ for some constant C . This then gives

$$\begin{aligned} &\sum_{m=0}^{M-1} \frac{1}{2\pi M} e^{-\frac{(x-r_n \cos(\alpha_m))^2 + (y-r_n \sin(\alpha_m))^2}{b^2}} \\ &= \sum_{m=0}^{M-1} \frac{1}{2\pi M} s(\alpha_m) \end{aligned} \quad (17)$$

$$= \int_0^{2\pi} s_n(\alpha) d\alpha + \epsilon(r_n) \quad (18)$$

where $|\epsilon(r)| \leq C(\sqrt{2} + \Delta)r/b^4 N^2$.

We now multiply by w_n and sum over n . Since the error term $\epsilon(r)$ can be bounded by a linear function in r and the Gauss–Jacobi quadrature integrates polynomials of degree $2M - 1$ exactly, we have

$$\left| \sum_{n=0}^{M-1} w_n \epsilon(r_n) \right| \leq \frac{C(\sqrt{2} + \Delta)}{b^4 N^2} \int_0^{\sqrt{2} + \Delta} r^2 dr \quad (19)$$

$$= \frac{C(\sqrt{2} + \Delta)^4}{b^4 N^2}. \quad (20)$$

What remains is thus to calculate

$$\sum_{n=0}^{N-1} w_n I(r_n), \quad (21)$$

where $I(r) = \int_0^{2\pi} s_n(\alpha) d\alpha$. For the Gauss–Jacobi quadrature rule used here, the error is proportional to

$$\frac{M!}{2M!} \left(\frac{(M+1)!}{(2M+1)!} \right)^2 I^{(2M)}(r) \quad (22)$$

for some $r \in [0, \sqrt{2} + \Delta]$. Our goal is therefore to bound the $2M$ th derivative of $I(r)$.

We first note that (x, y) can be written in a polar representation, obtaining $x = \rho \cos(\eta)$ and $y = \rho \sin(\eta)$ for $\rho \in [0, \sqrt{2}]$ and $\eta \in [0, 2\pi)$. This allows us to rewrite $I(r)$ in the following manner

$$I(r) = \int_0^{2\pi} e^{-\frac{(x-r\cos(\alpha))^2 + (y-r\sin(\alpha))^2}{b^2}} d\alpha \quad (23)$$

$$= \int_0^{2\pi} e^{-\frac{(r-\rho\cos(\alpha-\eta))^2}{b^2}} \cdot e^{-\frac{\rho^2 \sin^2(\alpha-\eta)}{b^2}} d\alpha \quad (24)$$

$$= \int_0^{2\pi} e^{-\frac{(r-\rho\cos(\alpha))^2}{b^2}} \cdot e^{-\frac{\rho \sin^2(\alpha)}{b^2}} d\alpha. \quad (25)$$

Setting $t(r) = e^{-\frac{(r-\rho\cos(\alpha))^2}{b^2}}$, we note that this is simply an affine transformation of the Gaussian function $r \mapsto e^{-r^2}$. Consequently, its derivatives can be expressed using Hermite polynomials. Specifically, if H_k is the k th Hermite polynomial, we have that

$$t^{(k)}(r) = \frac{(-1)^k}{b^k} H_k \left(\frac{r - \rho \cos(\alpha)}{b} \right) e^{-\frac{(r-\rho\cos(\alpha))^2}{b^2}}. \quad (26)$$

From standard bounds on H_k (DLMF, (18.14.9)), we obtain that

$$|t^{(k)}(r)| \leq \frac{\sqrt{2^k k!}}{b^k}. \quad (27)$$

Computing the k th derivative of $I(r)$, plugging in the above bound, and noting that the second factor in the integrand (which does not depend on r) is less than one, we obtain

$$|I^{(k)}(r)| \leq \frac{\sqrt{2^k k!}}{b^k}. \quad (28)$$

The Gaussi–Jacobi quadrature error can therefore be bounded by

$$\begin{aligned} & \frac{M!}{2M!} \left(\frac{(M+1)!}{(2M+1)!} \right)^2 \frac{\sqrt{2^{2M} 2M!}}{b^{2M}} \\ &= \frac{M!}{\sqrt{2M!}} \left(\frac{(M+1)!}{(2M+1)!} \right)^2 \left(\frac{2}{b^2} \right)^M \end{aligned} \quad (29)$$

$$\leq \left(\frac{M!}{2M!} \right)^2 \left(\frac{2}{b^2} \right)^M. \quad (30)$$

Combining these results, we obtain that

$$\begin{aligned}
& \sum_{n=0}^{N-1} \sum_{m=0}^{M-1} \frac{w_n}{2\pi M} e^{-\frac{(x-r_n \cos(\alpha_m))^2 + (y-r_n \sin(\alpha_m))^2}{b^2}} \\
&= \int_D e^{-\frac{(x-u)^2 + (y-v)^2}{b^2}} dudv \\
&+ O\left(\frac{(\sqrt{2} + \Delta)^2}{N^2 b^4} + \left(\frac{M!}{2M!}\right)^2 \left(\frac{2}{b^2}\right)^M\right)
\end{aligned} \tag{31}$$

for $D = \{(u, v) \mid u^2 + v^2 < (\sqrt{2} + \Delta)^2\}$. We now need to approximate this integral. To do this, we extend it to an integral over all of \mathbb{R}^2 , which gives the result πb^2 . To quantify the error in the approximation, we must therefore bound

$$\int_{\mathbb{R}^2 \setminus D} e^{-\frac{(x-u)^2 + (y-v)^2}{b^2}} dudv. \tag{32}$$

We again consider polar coordinates for both (x, y) and (u, v) , which transforms the above expression into

$$\begin{aligned}
& \int_{\sqrt{2} + \Delta}^{+\infty} \int_0^{2\pi} e^{-\frac{r^2 + \rho^2 - 2r\rho \cos(\alpha - \eta)}{b^2}} d\alpha dr \\
&= \int_{\sqrt{2} + \Delta}^{+\infty} e^{-\frac{r^2 + \rho^2}{b^2}} \int_0^{2\pi} e^{\frac{2r\rho \cos(\alpha)}{b^2}} d\alpha dr.
\end{aligned} \tag{33}$$

The innermost integral can be written as $2\pi I_0(2r\rho/b^2)$, where I_0 is the zeroth-order modified Bessel function of the first kind. This gives

$$2\pi \int_{\sqrt{2} + \Delta}^{+\infty} e^{-\frac{r^2 + \rho^2}{b^2}} I_0(2r\rho/b^2) dr. \tag{34}$$

Bounding $I_0(2r\rho/b^2)$ by $e^{2r\rho/b^2}$ (DLMF, (10.14.3)), we obtain the upper bound

$$\begin{aligned}
& 2\pi \int_{\sqrt{2} + \Delta}^{+\infty} e^{-\frac{r^2 + \rho^2}{b^2}} e^{\frac{2r\rho}{b^2}} dr \\
&= 2\pi \int_{\sqrt{2} + \Delta}^{+\infty} e^{-\frac{(r-\rho)^2}{b^2}} dr = 2\pi \int_{\sqrt{2} + \Delta - \rho}^{+\infty} e^{-\frac{r^2}{b^2}} dr.
\end{aligned} \tag{35}$$

Since $\rho \leq \sqrt{2}$, we have that $\sqrt{2} + \Delta - \rho \geq 0$, so we can bound this integral using standard results on the integral of a Gaussian function DLMF, (7.8.3) to obtain the bound

$$2\pi b e^{\frac{(\sqrt{2} + \Delta - \rho)^2}{b^2}} \leq 2\pi b e^{-\frac{\Delta^2}{b^2}}. \tag{36}$$

This, together with the quadrature error bounds, gives us that

$$\begin{aligned}
& \sum_{n=0}^{N-1} \sum_{m=0}^{M-1} \frac{w_n}{2\pi M} e^{-\frac{(x-r_n \cos(\alpha_m))^2 + (y-r_n \sin(\alpha_m))^2}{b^2}} \\
&= \pi b^2 \\
&+ O\left(\frac{(\sqrt{2} + \Delta)^2}{N^2 b^4} + \left(\frac{M!}{2M!}\right)^2 \left(\frac{2}{b^2}\right)^M + b e^{-\frac{\Delta^2}{b^2}}\right)
\end{aligned} \tag{37}$$

Plugging this into our expression for $P^T P x$ then gives us the desired result. \square

Because of the above result, we can reconstruct x by solving the deconvolution problem in equation 10. This can be done in several ways, most easily by approximating the discrete convolution with a circular convolution and solving it by pointwise division in the Fourier domain (Bertero et al., 2021). To ensure that this deconvolution problem is relatively well-posed, however, the Fourier transform of ϕ must not decay too fast – in other words, we cannot choose b to be too small. We have found that choosing b on the order of $1/L$ results in a well-conditioned deconvolution problem.

B Properties of ϕ

Proposition 1 shows that P is an approximate isometry when restricted to smooth images. Indeed, we can show that $\phi[i, j] = (\pi b^2 L^2)^{-1} e^{-\frac{i^2+j^2}{b^2 L^2}}$ is a lowpass filter which sums to one.

For this, we use the Poisson summation formula (Stein & Weiss, 1971, Chapter VII.2). First, we note that the Fourier transform of the continuous function

$$\phi(u, v) = \frac{1}{\pi b^2 L^2} e^{-\frac{u^2+v^2}{b^2 L^2}} \quad (38)$$

is given by

$$\widehat{\phi}(\omega, \xi) = e^{-\pi^2 b^2 L^2 (\omega^2 + \xi^2)}. \quad (39)$$

We thus have

$$\begin{aligned} \sum_{i,j=-\infty}^{+\infty} \phi[i, j] &= \sum_{i,j=-\infty}^{+\infty} \phi(i, j) \\ &= \sum_{k,\ell=-\infty}^{+\infty} \widehat{\phi}(k, \ell) \end{aligned} \quad (40)$$

$$= 1 + \sum_{k,\ell \neq 0} e^{-\pi^2 b^2 L^2 (k^2 + \ell^2)}. \quad (41)$$

Provided that b is large enough, the infinite sum is negligible (for $b = 1/L$, the largest term is of the order 10^{-4}). We thus have the desired result.

This in turn then means that

$$(Py)^T(Px) = y^T P^T P x \approx y^T (x \star \phi) \approx y^T x. \quad (42)$$

for two smooth images x and y .

To prove stability, we note that since the Fourier transform of ϕ has its largest value close to one, the largest eigenvalue of $P^T P$ is also close to one, which means that $\|P\| \approx 1$.

C Computational complexity of polar mapping

In terms of computational cost, application of P and P^T can be implemented efficiently using fast Gaussian gridding (Greengard & Lee, 2004; Barnett et al., 2019; Shih et al., 2021). As a result of this, the number of non-negligible terms in equation 4 and its adjoint is $\mathcal{O}(1)$, which means that both operations can be computed in $\mathcal{O}(L^2)$ time (recall that $N = \mathcal{O}(L)$ and $M = \mathcal{O}(L)$). Finally, the deconvolution step, if implemented using FFTs, has a computational cost of $\mathcal{O}(L^2 \log L)$. Mapping between Cartesian and polar domains can thus be achieved quite efficiently.

D Angular attention

We can examine the behavior of the angular attention mechanism by studying the attention coefficients for a pair of projection images. One image is the rotated version of another and both are subjected to varying levels of noise. By running these through the polar transformer, we can record the attention coefficients and plot them according to the angular index ℓ . The results are shown in Figure 4.

At high SNR, the attention coefficients are concentrated around the true rotation angle, showing that the angular attention mechanism successfully aligns the two images with respect to one another. As the noise increases, however, the attention coefficients are dispersed over a wider range of angles, reflecting the increased uncertainty about the angular registration. Importantly, however, this is a robust degradation in the sense that the attention coefficients of high magnitude are still located around the true angle.

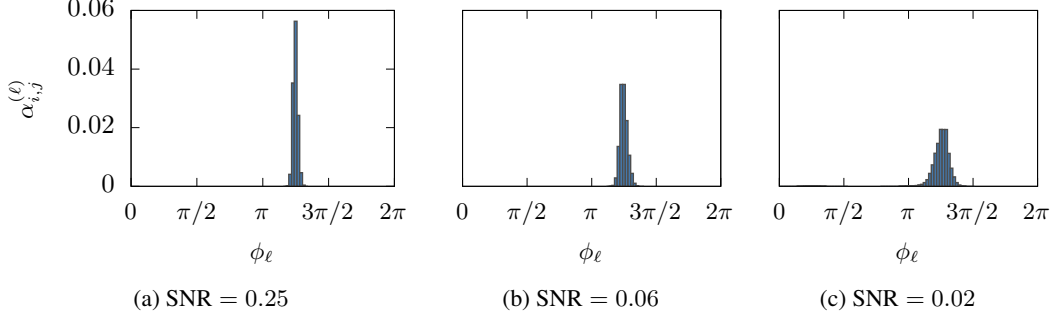


Figure 4: The angular attention coefficients for a pair of images at different noise levels are shown. For high SNR (a), we see high concentration around the true angle, while at lower SNR (b,c), there is more uncertainty regarding the correct angular assignment.

E Attention for Clustering

The polar transformer architecture is designed to combine information from precisely those image in an input set which match up to plane rotation. It is the process of finding out which ones these are that we call clustering.

How it occurs can be observed by studying the activations in the activation coefficient matrix as a set with known split of two directions is processed. Without loss of generality (because the attention mechanism is equivariant under permutations of the images), this can be realized by taking the first 8 projections in one directions and the remaining 8 projections in another direction. Ideally, the attention (summed over the angular direction) should then have block-matrix structure, as only the images corresponding to the same direction interact with each other. Indeed this matches the observations in the case of relatively high SNR (see Figure 6). Consequently, the model can then also combine information for denoising purposes just as well as if the directions had already been known a priori, as is the case of a directional set. This manifests in MSE scores that are almost as good with two directions as with a single direction (Figure 2a).

At lower SNR meanwhile, the attention mechanism cannot be as confident in classifying the directions anymore and the block structure of the matrix is more fuzzy. This manifests in MSE values that are not quite as good anymore as in the ideal predetermined case, but there is still more information to be exploited even from the uncertain classification as from only single images and thus even the clustering model still denoises better at low SNR than single-image models can.

F More denoising examples

More examples of denoising results for the standard noise configuration and the CTF-filtered and shifted images are shown in Figure 5.

G Poisson noise parametrization

For Gaussian noise, we used white Gaussian noise at a fixed noise level that was added to the images. Poisson noise meanwhile is a quantization process, which does not directly match the notion of separate signal and noise level. It can however be unified by introducing a *Poissonicity* parameter η which controlled the extent to which it approached a Gaussian noise (which occurred as $\eta \rightarrow 0$).

The (discrete) Poisson distribution has one parameter λ and a probability mass function of

$$\text{PMF}_{\text{Pois}(\lambda)}(k) = \lambda^k \frac{e^{-\lambda}}{k!} \quad (43)$$

The mean of this distribution is again λ , and the standard deviation $\sqrt{\lambda}$.

To use the Poisson distribution directly as a source of shot noise would require comparing concrete finite electron counts, which is inconvenient for comparison with the Gaussian setting as that corre-

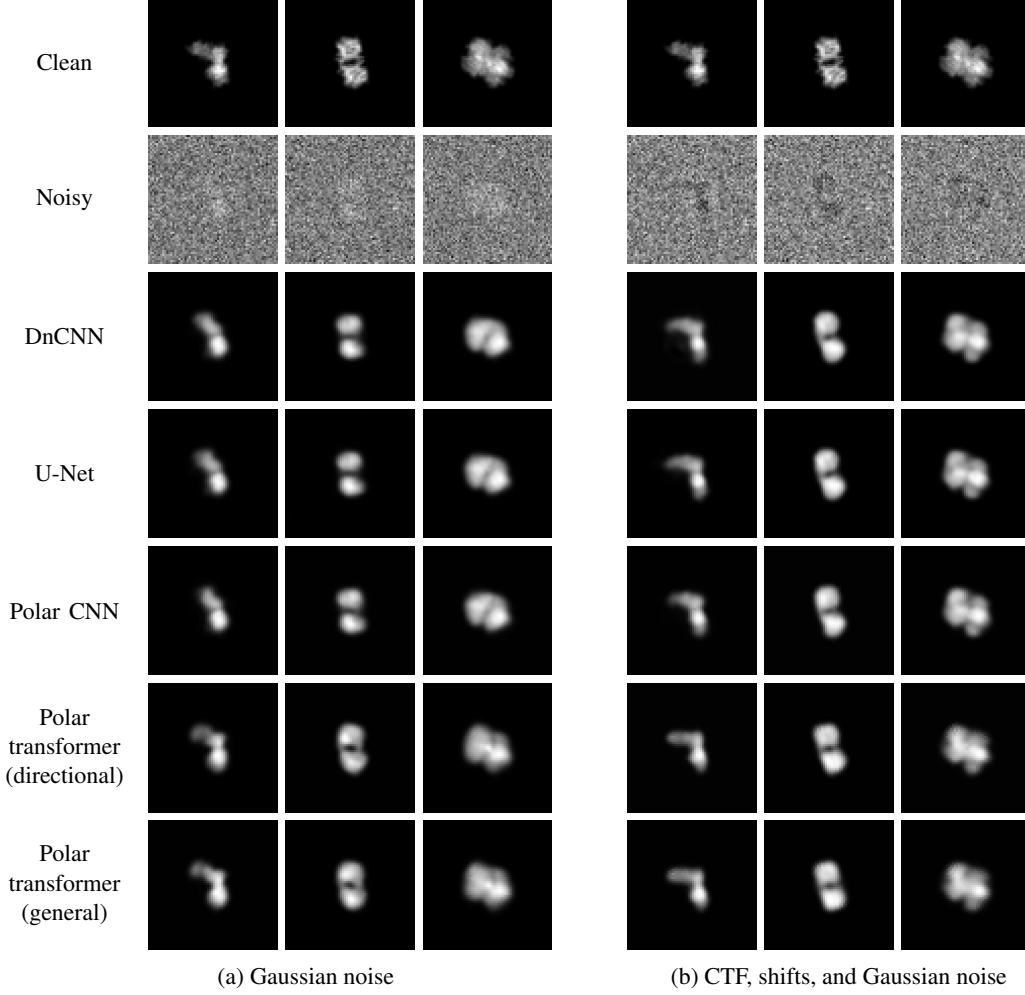


Figure 5: More denoising examples for two noise configurations: (a) the standard projection model plus Gaussian noise with $\text{SNR} = 0.03$ and (b) the standard projection model with CTF (defocus values in the range 15000 Å to 25000 Å and shifts (of magnitude at most 8 pixels) with $\text{SNR} = 0.02$.

sponds to infinite electron rate. Also, the Poisson expectation is always positive, whereas we use by convention noise that is symmetric about zero in the regions where the electron beam is unobstructed by molecules (the background).

We therefore define a slightly different process to emulate shot noise, which has initially two parameters η and λ_0 . Given an input signal x which is close to zero in the background, let

$$y = \eta \cdot (\lambda_0 - c), \quad (44)$$

with

$$c \leftarrow \text{Pois}(\lambda_0 - x/\eta). \quad (45)$$

The subtraction $\lambda_0 - x/\eta$ expresses that positive x attenuates the pixel-wise dose, corresponding to blocking of the electrons by the molecule (more accurately, destructive interference due to phase shift). Note that the opposite behavior can be achieved by choosing negative η .

Then the noisy image has in the background again mean 0, matching the mean in the Gaussian case, and standard deviation

$$N = \sqrt{\lambda_0} \cdot \eta. \quad (46)$$

The local perturbation of the mean due to x has unity gain (because the multiplication by η in equation 44 is canceled by division in equation 45).





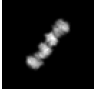



(Clean)	(Poisson)	Denoiser:	
		Gaussian polar tfmr. (dir.)	Poisson polar tfmr. (dir.)
			
			
		0.043	0.038
		Mean	
		MSE	

Table 1: Example results like in Figure 2b, but for Poisson noise. SNR of 0.03 by the notion of Equation 47. A transformer model that has been trained on Gaussian noise is compared with one trained on Poisson noise.

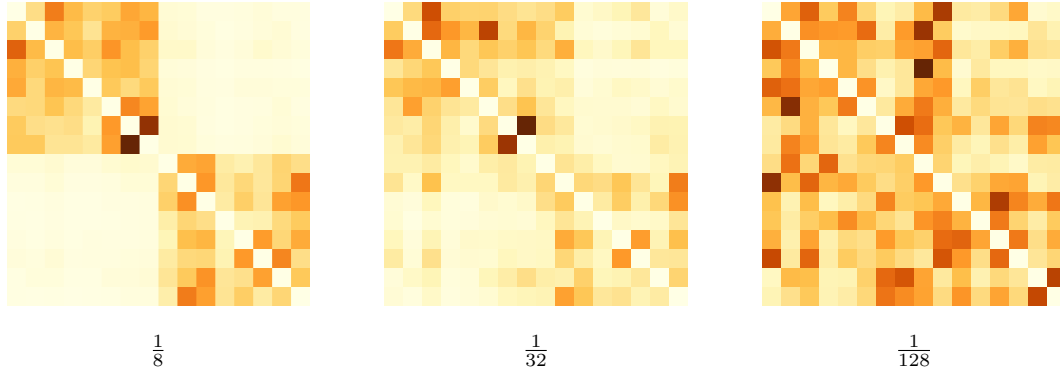


Figure 6: Example attention matrices for a 2-direction, 16-image-set polar transformer model at different SNR levels.

We want N to match the noise’s standard deviation in the Gaussian setting, which is by convention represented as

$$N = \frac{S}{\sqrt{\text{SNR}}}. \quad (47)$$

This can be fulfilled by solving equation 46 for λ_0 , which gives

$$\lambda_0 = \frac{S^2}{\text{SNR} \cdot \eta^2}. \quad (48)$$

η remains as a parameter. If $\eta \approx 0$ is chosen, λ_0 approaches infinity. A Poisson distribution with large λ is well approximated by a Gaussian distribution, in that sense the results can directly be compared.

H Extension to experimental data

To demonstrate the potential of the proposed polar transformer, we have evaluated the model on various synthetic datasets. In order to apply it to practical cryo-EM datasets, however, further work must be conducted.

The first challenge is to scale the model to handle larger sets of images – thousands or hundreds of thousands of images in a single set. In order to train models for such large sets, a more sophisticated training protocol is needed that better manages the computational burden. It is likely, however, that

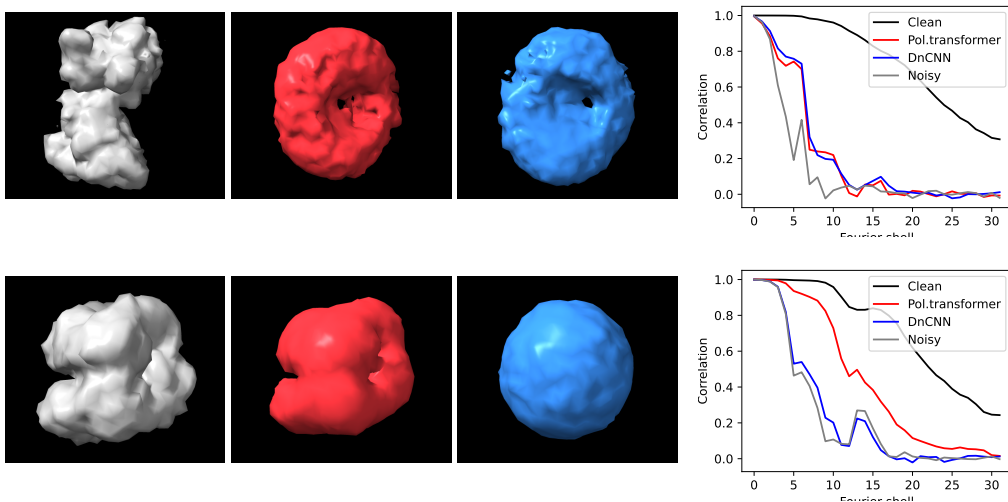


Figure 7: Reconstruction quality like in Figure 3, but for molecules with PDB IDs 1T5C (top) and 1V8C (bottom).

the effect of the set size on training performance will saturate at some level. Indeed, the construction of the polar transformer is not dependent on a specific set size and can in theory be applied to sets of any size. This will allow the trained model to be applied to larger sets during the evaluation (inference) step.

The second challenge is to train on more realistic data. This can be achieved in two ways: more realistic simulations and self-supervised learning. The former would involve using a digital twin, such as Parakeet (Parkhurst et al., 2021), to generate more realistic training sets by multislice simulation. However, while this simulation is better than a projection-based simulation with Gaussian noise, it still falls short of modeling experimental data. It will therefore have to be combined with some type of self-supervised training on experimental datasets. Here, individual projection images can be extracted from EMPIAR database (Iudin et al., 2022) to yield a large training set. By using alternating video frames, a noise2noise training paradigm (Lehtinen et al., 2018) may be applied as illustrated in Bepler et al. (2020). Alternatively, the use of masking and specialized loss functions could allow for training the denoiser even in the absence of video frames.

Both of these represent important avenues for future work in realizing the full potential of the polar transformer.

I More 3D reconstruction results

In Section 6.5 it was demonstrated that the improved denoising our method provides can also lead to better 3D reconstructions. Figure 7 shows the FSCs for reconstructions of two other molecules: CENP-E (PDB ID 1T5C) and a MoaD protein (PDB ID 1V8C).

We note that for 1V8C, the polar transformer yields a more accurate reconstruction, but that 1T5C, the performance is similar to that of DnCNN. There are a few potential reasons for this. First, we are working with only 2 048 projections, which means that certain viewing directions may not be very well represented. Second, the clustering algorithm may result in sets where images close to the center of the cluster have a viewing direction close to that of the others, but images close to the edge of the cluster have higher error. As a result, those images will contribute to a lower-quality reconstruction. Third, the clustering algorithm only operates on a hemisphere (combining antipodal viewing directions together), which creates a bias for viewing directions close to the equator.

We also note that these reconstructions are not truly ab initio, since prior knowledge of the viewing directions were used to cluster the images. That being said, it is an approximation of what would be achieved using standard 2D classification methods, such as bispectrum-based approaches (Zhao &

Singer, 2014b). It therefore provides an indication of the performance of 3D reconstruction from the denoised images. A full reconstruction pipeline incorporating our method still requires improving several aspects, which will need to be addressed in future work.